Nano Energy 70 (2020) 104508

Contents lists available at ScienceDirect

Nano Energy

journal homepage: http://www.elsevier.com/locate/nanoen

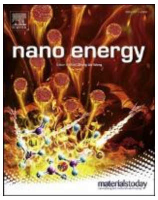

A carbon-doped tantalum dioxyfluoride as a superior electron transport material for high performance organic optoelectronics

Maria Vasilopoulou [a,*], Abd Rashid Bin Mohd Yusoff [b], Navaratnarajah Kuganathan [c, d], Xichang Bao [e], Apostolis Verykios [a,f], Ermioni Polydorou [a,f], Konstantina-Kalliopi Armadorou [a,g], Anastasia Soultati [a], Georgios Papadimitropoulos [a], Muhammad Irfan Haider [h,i], Azhar Fakharuddin [h, 1], Leonidas C. Palilis [f], Stella Kennou [j], Alexander Chroneos [c, d], Panagiotis Argitis [a], Dimitris Davazoglou [a]

[a] Institute of Nanoscience and Nanotechnology, National Center for Scientific Research "Demokritos", 15341, Agia Paraskevi, Attica, Greece
[b] Department of Physics, Swansea University, Vivian Tower, Singleton Park, SA2 8PP, Swansea, United Kingdom
[c] Department of Materials, Imperial College London, London, SW7 2AZ, UK
[d] Faculty of Engineering, Environment and Computing, Coventry University, Priory Street, Coventry, CV1 5FB, United Kingdom
[e] Qingdao Institute of Bioenergy and Bioprocess Technology, Chinese Academy of Sciences, Qingdao, 266101, China
[f] Department of Physics, University of Patras, 26504, Patras, Greece
[g] Department of Chemistry, National and Kapodestrian University of Athens, 15771, Zografos, Greece
[h] Department of Physics, University of Konstanz, 78457, Konstanz, Germany
[i] Department of Chemistry, University of Wah, 47040, Wah, Pakistan
[j] Department of Chemical Engineering, University of Patras, 26504, Patras, Greece

ARTICLE INFO

Keywords:
Tantalum oxyfluorides
Carbon doping
Organic light emitting diodes
Organic solar cells
Non-fullerene acceptors
Electron transport layer

ABSTRACT

The design and development of novel materials with superior charge transport capabilities plays an essential role for advancing the performance of electronic devices. Ternary and doped oxides can be potentially explored because of their tailored electronic energy levels, exceptional physical properties, high electrical conductivity, excellent robustness and enhanced chemical stability. Here, a route for improving metal oxide characteristics is proposed by preparing a novel ternary oxide, namely, carbon-doped tantalum dioxyfluoride (TaO_2FC_x) through a straightforward synthetic route and exploring its effectiveness as an electron transport material in optoelectronic devices based on organic semiconductors. Among other devices, we fabricated fluorescent green organic light emitting diodes with current efficiencies of 16.53 cd/A and single-junction non-fullerene organic solar cells reaching power conversion efficiencies of 14.14% when using the novel oxide as electron transport material. Our devices also exhibited the additional advantage of high operational and temporal stability. Non-fullerene OSCs based on the novel compound showed unprecedented stability when exposed to UV light in air due to the non-defective nature of TaO_2FC_x. We employed a tank of experiments combined with theoretical calculations to unravel the performance merits of this novel compound. This study reveals that properly engineered ternary oxides, in particular, TaO_2FC_x or analogous materials can enable efficient electron transport in organic optoelectronics and are proposed as an attractive route for the broader field of optoelectronic devices including metal-organic perovskite, colloidal quantum dot and silicon optoelectronics.

1. Introduction

Optoelectronic devices using solution-processed semiconductors, such as organic semiconductors and halide organic-inorganic perovskites, are the frontrunners in near future applications on the areas of solid-state lighting and solar energy conversion due to their low-cost and enhanced performance [1,2]. Solution-processable organic semiconductor-based devices, such as organic light emitting diodes

---

* Corresponding author.
E-mail address: m.vasilopoulou@inn.demokritos.gr (M. Vasilopoulou).
[1] IMEC Kapeldreef 75, Heverlee 3001, Belgium (present affiliation).

https://doi.org/10.1016/j.nanoen.2020.104508
Received 19 September 2019; Received in revised form 13 January 2020; Accepted 15 January 2020
Available online 18 January 2020
2211-2855/© 2020 Published by Elsevier Ltd.

(OLEDs) and organic solar cells (OSCs), continue to draw large interest due to their high stability and non-toxicity [3,4]. These, combined with the renaissance that OSCs witnessed in recent years with the advent of non-fullerene acceptors make them a competitive choice for real-life applications. However, the tremendous recent progress in OLEDs and OSCs has been accomplished not only by the development of novel semiconductors for the active layer (emitter/absorber), such as non-fullerene acceptors, but also by the adoption of more advanced and sophisticated device architectures [5–9]. Their market entry, however, requires further improvements in efficiency and, more importantly, a longer operational stability. A critical aspect towards enhanced device performance is the carrier injection/transport efficiency from the electrodes to the organic semiconductor in OLEDs and vice versa in OSCs. Particularly, the electron transport layer (ETL) is indispensable to achieving high electron transfer rates from/to the cathode electrode hence maximizing the device efficiency [10,11]. Besides appropriate energy levels to form a type II (i.e. staggered gap) heterojunction with the organic semiconductor used in the active layer, an ideal ETL must also possess an adequate n-type conductivity, a low refractive index to enhance the out-coupling efficiency (in OLEDs), chemical and physical robustness, high hydrophobicity to restrict water adsorption on the organic semiconductor surface and prolong device stability [12,13]. In devices with regular (i.e. p–i–n) architecture, the latter is highly crucial to avoid moisture penetration into the active organic layer before cathode deposition. Various types of electron transport materials, such as alkali-earth metals [14], polyamine compounds [15], polyelectrolytes [16], poly(ionic liquids) [17], and metal salts and bases [18], have been developed. Remarkably, research on the intrinsically robust and environmental stable inorganic transition-metal oxides as ETLs in organic and related perovskite optoelectronics is scarce although there are more than 4000 ternary metal oxides catalogued in the Inorganic Crystal Structure Database (ICSD). The highly defective zinc oxide (ZnO), titanium dioxide (TiO_2) and the less-defective tin oxide (SnO_2) are the most employed metal oxides (in pristine form and doped) reported so far [19–21]. The former both are known to induce degradation due to chemical reaction (derived from their photocatalytic activity) at their interfaces with organic/perovskite layers thereby making them not suitable for long-term stable devices [22]. Recently, some alternative ternary oxides such as the La-doped $BaSnO_3$ [23], and the $PbZrTiO_3$ ferroelectric oxide [24], have been successfully applied as electron extraction materials in perovskite solar cells. However, future optoelectronic devices targeting technological applications urgently require the extensive exploration of next generation of metal oxide-based charge transport interlayers to simultaneously enhance stability and device efficiency [25].

Tantalum pentoxide (Ta_2O_5) is a non-defective wide bandgap material with a large refractive index, high thermal tolerance and chemical stability under various environments. It has attracted considerable attention as a high dielectric constant gate oxide for field-effect transistors and resistive memories as well as in coatings and photocatalytic devices [26]. However, the large optical bandgap (larger than 4.0 eV) and extremely poor electrical conductivity render stoichiometric Ta_2O_5 highly unsuitable as charge transport material for modern applications, such as in solar energy to electricity conversion and solid-state lighting. Wan et al. reported that Ta sub-oxide (TaO_x) is a promising electron selective contact for crystalline silicon (Si) photovoltaics and photoelectrochemical water reduction [27]. Tantalum oxynitride (TaON) [28], dioxychloride (TaO_2Cl) [29], and dioxyfluoride (TaO_2F) [30], and the MXene family member tantalum hemicarbide (Ta_2C) [31], are excellent electrocatalysts for several catalytic reactions because of their suitable optical bandgap and superior charge transfer rates. Among these electrocatalysts, TaO_2F is the one of the most stable inorganic compounds found in nature because it exhibits one of the highest known melting points between existing materials [30,32]. Furthermore, carbon (C) doping has been found to simultaneously improve stability as well as light harvesting and charge separation efficiency of many compounds possessing photocatalytic activity [33–35]. These observations motivated us to design and develop a novel ternary compound with exceptional physical and optoelectronic properties. This novel carbon-doped tantalum dioxyfluoride (TaO_2FC_x) exhibits well-matched energy levels with those of most organic semiconductors, high electron conductivity, extremely low refractive index and high hydrophobicity, therefore, representing an ideal choice for the cathode interface of several types of optoelectronic devices. As a proof of concept, we apply our novel compound in OLEDs and OSCs with diverse architectures and organic active materials.

2. Experimental section

Preparation of TaO_2FCx. TaO_2FC_x films were deposited in a MOCVD home-made reactor [36,37], by using TaO_x and hexafluoroacetone (C_3F_6O, purchased from Sigma-Aldrich) vapours. TaO_x vapours were produced by heating a superficially oxidized metallic (Ta) filament (purchased from Merck) at 1000 °C. The C_3F_6O vapour was introduced in the deposition chamber by (10 sccm) N_2 stream bubbling through a saturator maintained at 60 °C. For the deposition, substrates were loaded on a copper susceptor (fixed between two Cu current leads) located 5 cm below the filament. The chamber was evacuated to 10^{-2} Torr, and the gases were inserted (flow of 100 sccm of N_2 and C_3F_6O vapours), followed by automatic pressure stabilisation to 1 Torr with the aid of a pressure control system consisting of a baratron manometer and an automatically driven butterfly valve. Finally, the filament was heated with the application of an AC (50 Hz) current to produce the TaO_x vapours. Bias voltage and deposition time were used to control film thickness with time varying between 1 and 60 s. The deposition of a pristine TaO_x was performed in a N_2 environment without the introduction of C_3F_6O vapours inside the chamber. During deposition, the substrate was near room temperature.

Theoretical methodology. All calculations were performed using dispersion corrected density functional theory as implemented in the VASP code, which solves the standard Kohn–Sham equations by using plane wave basis sets. For the exchange correlation energy term, the generalised gradient approximation was used in the form of the PBEsol functional. The standard projected augmented wave potentials and a plane-wave basis set with a cut off value of 500 eV were employed. A 4 × 2 × 4 Monkhorst–Pack k point mesh, which yielded 20 k points, was used in all calculations. The valence electronic configurations for Ta, O and F were $5p^6 6s^2 5d^3$, $2s^2 2p^4$ and $2s^2 2p^5$, respectively. Structural optimisations were performed using a conjugate gradient algorithm, and the forces on the atoms were obtained from the Hellmann–Feynman theorem, including Pulay corrections. In all optimised structures, forces on the atoms were smaller than 0.001 eV/Å. In this work, dispersion was included using the pair-wise force field, as implemented by Grimme et al. in the VASP package [38].

OLED devices fabrication and characterization. OLEDs with a forward (regular) architecture were fabricated on indium tin oxide (ITO) coated glass substrates (having a sheet resistance of 20 Ω/sq), which served as the transparent anode electrode. Prior to the organic emissive semiconductor deposition, the substrates were sequentially sonicated in acetone, 2-propanol and DI water for 10 min and then dried in a N_2 flow. The substrates were then treated with O_2 plasma for 10 min, followed by spin-coating of a thin (~40 nm) layer of poly(3,4-ethylenedioxythiophene) polystyrene sulfonate (PEDOT-PSS) (1.3 wt% dispersion in H_2O filtered with a 0.45 μm PVDF filter) (purchased from Sigma Aldrich) in ambient conditions at 7000 rpm for 40 s. PEDOT:PSS was annealed at 130 °C for 30 min to remove water residuals. The emissive layer (for the green OLEDs we used poly[(9,9-dioctylfluorenyl-2,7-diyl)-co-(1,4-benzo-2,1′,3-thiadiazole)] (F8BT, 9:1 F8:BT ratio) and for the blue OLEDs the blue emitting poly[2-(6-cyano-6′-methylheptyloxy)-1,4-phenylene] (CN-PPP]), both purchased from American Dye Source) was then spin coated onto PEDOT-PSS from a 10 mg mL^{-1} chloroform solution (filtered through a 0.22 μm PTFE filter) at 1200 rpm for 40 s to form a ~70 nm layer. The F8BT film was then annealed at 95 °C for 10 min (CN-PPP was annealed at 80 °C) to improve its morphology. In the control OLEDs, a thin caesium carbonate (Cs_2CO_3, purchased from Sigma-Aldrich) layer was deposited onto the organic emissive layer by spin coating at 2000 rpm for 40 s from a 5 mg mL^{-1} methanol solution to serve as the electron injection layer. For the deposition of TaO_2FC_x, some devices were transferred to the dedicated deposition chamber. The OLED structure was completed with the deposition of a 150 nm aluminum cathode (in a dedicated thermal evaporator) by using a shadow mask. Current density-voltage characteristics of OLEDs were measured with a Keithley 2400 source-measure unit whereas luminance and electroluminescence (EL) spectra were recorded with an Ocean Optics USB 2000 fiber optic spectrophotometer (assuming a Lambertian emission profile). All measurements were carried out in air at room temperature.

OSC device fabrication and characterization. Forward architecture OSCs were fabricated on PEDOT-PSS deposited on ITO/glass substrates that were prepared with the protocol reported in the previous section. The substrates were subsequently transferred to an argon filled glove box for photoactive layer deposition. The non-fullerene acceptor-based OSCs were fabricated using a poly[(2,6-(4,8-bis(5-(2-ethylhexyl-3-fluoro)thiophen-2-yl)-benzo[1,2-b:4,5-b′]dithiophene))-alt-(5,5-(1′,3′-di-2-thienyl-5′,7′-bis(2-ethylhexyl)benzo[1′,2′-c:4′,5′-c′]dithiophene-4,8-dione)]:3,9-bis(2-methylene-((3-(1,1-dicyanomethylene)-6,7-difluoro)-indanone))-5,5,11,11-tetrakis(4-hexylphenyl)-dithieno[2,3-d:2′,3′-d′]-s-indaceno[1,2-b:5,6-b′]dithiophene (PM6:IT-4F) organic absorber (both materials were purchased from Ossila). PM6:IT-4F blend was dissolved in chlorobenzene (CB) at a concentration of 20 mg/ml (1:1 wt ratio) and stirred at 50 °C for 5 h. Prior to spin coating, 1,8-diiodooctane (DIO) (0.6%, v/v) was added to the solution. Films were spin coated at 1700 rpm for 60 s and then annealed at 100 °C for 10 min. For the fullerene-based OSCs a poly[4,8-bis(5-(2-ethylhexyl)thiophen-2-yl) benzo[1,2-*b*;4,5-*b*′]dithiophene-2,6-diyl-*alt*-(4-(2-ethylhexyl)-3-fluorothieno[3,4-*b*]thiophene-)-(2-carboxylate-2-6-diyl)]: phenyl-C_{71}-butyric acid methyl ester (PTB7-Th:PC_{71}BM) organic absorber was used. The PTB7-Th:PC_{71}BM blend (both purchased from Ossila) was dissolved in 1,2 dichlorobenzene (*o*-DCB) at a concentration of 25 mg/ml (1:1.5 wt ratio) and stirred at 60 °C for 5 h. Prior to spin-coating, DIO (3%, v/v) was added to the solution. PTB7-Th:PC_{71}BM films were spin coated at 1000 rpm for 90 s and left to dry for 30 min. The control samples were covered with a perylene diamide amino N-oxide (PDINO) ETL spin-coated from a 5 mg/ml methanol at 2000 rpm for 40 s, whereas the samples with TaO_2FC_x were immediately transferred from the glove box to the dedicated deposition chamber. OSCs were completed with the thermal evaporation of an Al electrode with a shadow mask defining the active cell area. For the inverted architecture OSCs, a 30 nm-thick ETL was deposited on pre-cleaned and O_2 plasma-treated fluorinated tin oxide (FTO) substrates. A ZnO ETL was formed for the reference inverted devices by spin-coating from a 0.5 mol/L $ZnC_4H_6O_4$ solution in ethanolamine and 2-methoxyethanol, which was then heated at 200 °C for 30 min. The TaO_2FC_x layer was deposited as described above, followed by the deposition of the PM6:IT-4F blend and 10 nm-thick MoO_x capped with a 150 nm Al anode. The cell active area was fixed at 12.56 mm^2 by the use of a shadow mask. Solar cell optoelectronic characterization was performed as reported elsewhere [39].

Electron mobility calculations. For the calculations of the electron mobility of both the PM6:IT-4F and PTB7-Th:PC_{71}BM blends we fabricated electron-only devices with the structure ITO/active absorber/ETL/Al and recorded the current density-voltage (J–V) characteristics. These were fitted in the space charge limited conduction regime with the Mott–Gurney law, including the Frenkel effect on the electric field dependent mobility, as given by the equation:

$$J = (9/8)\varepsilon_0\varepsilon_r\mu_0\exp[0,89\beta\{(V/d\}^{1/2}](V^2)/(d^3), \tag{1}$$

For current density J, applied voltage V, free space permittivity ε_0, relative blend permittivity ε_r (e_r ¼ 3.5), zero-field electron mobility μ_0, field activation factor β and active layer thickness d (d ¼ 80 nm). The fitting parameters μ_0 and β are listed in Tables S4 and S6, respectively, and were extracted from the intercept and slope of the J vs. $V^{1/2}$ plot.

Additional characterization. X-ray photoelectron spectroscopy (XPS) and ultra-violet photoelectron spectroscopy (UPS) measurements characterized the surface chemical composition and the electronic structure of TaO_2FC_x films deposited on ITO/glass or on an F8BT coated PEDOT-PSS/ITO on glass substrate. An unmonochromatised Mg Ka line at 1253.6 eV (12 keV with 15 mA anode current) and an analyzer (Leybold EA-11) pass energy of 100 eV, which gives a full width at half maximum (FWHM) of 1.3 eV for the Au 4f $_{7/2}$ peak, were used for the XPS measurements, whereas XPS analysis was performed at 0° take-off angle. In all XPS spectra the binding energy (BE) of the predominant aliphatic contribution to the C 1s peak at 284.8 eV was used as a measured BE reference. The analyzed area was approximately a 2 × 5 mm^2 rectangle positioned near the geometric centre of each sample. The UPS measurements (that was taken first followed by XPS measurements) were performed using the He I (21.2eV) excitation line, and a voltage of 12.23 V that was applied to the specimen to separate the high BE cut-off from the analyzer. The composition and crystallinity of ternary oxide films were studied with an X-ray Siemens D-500 diffractometer. UV–Vis transmittance/absorption measurements were recorded using a PerkinElmer Lambda 40 UV/Vis spectrometer. The surface topographies/morphologies were prompted with NT-MDT AFM and a JEOL 7401f FESEM.

3. Results and discussion

Fig. 1a illustrates the preparation of the ternary compound. Tantalum oxide (TaO_x) vapours were produced by heating a superficially oxidized tantalum filament and then reacted with hexafluoroacetone (C_3F_6O) vapours introduced inside the deposition chamber by bubbling of a nitrogen (N_2) stream through a saturator kept at 60 °C. The ternary material was deposited as a thin film on top of selected substrates at room temperature. XPS and UPS photoelectron spectroscopies were employed to reveal the chemical composition (i.e. stoichiometry), valence band (VB) position and work function (W_F) of the material, which are all highly critical to its application as an electron selective layer. Fig. 1b depicts the Ta 4f XPS core levels, which consist of two different doublet peaks attributed to Ta $4f_{7/2}$ and Ta $4f_{5/2}$. In the first doublet, the Ta $4f_{7/2}$ peaks at 26.2 eV and is attributed to the stoichiometric oxide phase [40]. The second doublet is shifted to high energies, and the Ta 4f $_{7/2}$ appears at 26.9 eV [41]. This doublet is assigned to a fluorinated oxide phase, and the shift to high energies is due to the high fluorine anion electronegativity [42]. The F 1s spectrum (Fig. 1c) was fitted with two Gaussians peaked at 688.1 and 684.8 eV attributed to fluorine anions bonded to Ta and C, respectively [43,44]. This finding indicates the incorporation of C within the structure of the developed material. The O 1s spectrum (Fig. 1d) was also fitted with two Gaussians, one peaked at 530.6, which is attributed to Ta–O bonds, and a second peaked at 531.7 eV, corresponding to –OH groups due to surface contamination. Fig. 1e depicts the high binding energy cut-off region (left), the full VB (middle) and the near Fermi level region (right) of the UPS spectrum of TaO_2FC_x. The VB maximum appears at 2.9 eV below the Fermi level, whereas the W_F is 4.5 eV. No bands appear inside the band gap, suggesting that the synthesised material is non-defective. The developed material exhibits a lower bandgap than the pristine TaO_x deposited in O environment (Figs. S1a and S2a, Supporting Information). However, it remains highly transparent (Fig. S1b), which is highly desirable for its application at the bottom cathode transparent electrode of inverted devices. In the X-ray diffraction pattern (Fig. 1f), three crystalline peaks appear at 2θ the positions of 33°, 62° and 67°. These peaks are characteristic of TaO_2F [45,46]. We found that the TaO_x deposited without the injection of C_3F_6O is completely amorphous (Fig. S3). Additionally, the fluorinated oxide exhibits an extremely low

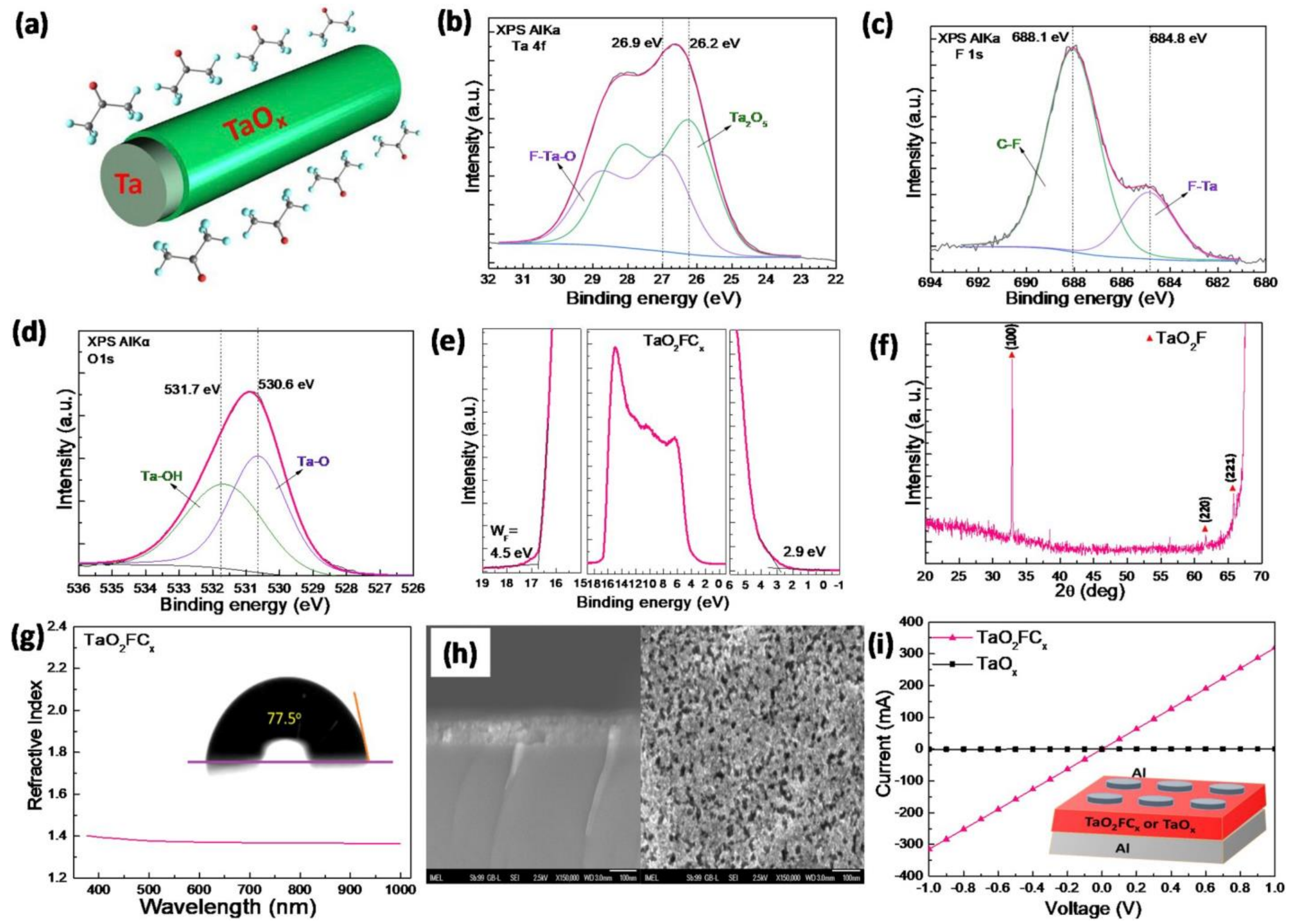

Fig. 1. (a) Schematic illustration of the synthetic procedure of TaO_2FC_x. (b) Ta 4f, (c) F 1s and (d) O 1s XPS peaks of the carbon-doped tantalum dioxyfluoride film deposited on ITO substrate. (e) UPS spectrum of the same film. (f) X-ray diffraction pattern, (g) measured refractive index and (h) SEM topography of the TaO_2FC_x film deposited on silicon substrate. The water contact angle measurement of this film is shown as inset in Fig. 1g. (i) Current-voltage characteristics of the device with a structure $Al/TaO_2FC_x/Al$ (shown as inset). The corresponding characteristic curve of the $Al/TaO_x/Al$ device structure is also shown for comparison.

refractive index of approximately 1.4 in the visible and near-IR region (Fig. 1g), which is attributed to its high fluorine content [47]. The refractive index of the pristine oxide is approximately 2.0 (Fig. S4) according to literature [48]. The surface topography of the ternary compound is grain-like (Fig. 1h) with the grain size, thickness (Fig. S5), porosity (Fig. S6) and surface roughness (Fig. S7) precisely controlled by changing the deposition environment, bias voltage applied on the Ta wire and deposition time. These changes, however, do not significantly affect the stoichiometry (Figs. S8 and S9) hence offering a large window for potential material applications that require either a compact thin layer (i.e. organic and related optoelectronics) or a thick porous material (i.e. catalysis, energy storage devices and beyond). The high fluorine content also resulted in an increased hydrophobicity of the synthesised material (inset, Fig. 1g), especially when compared to the pristine oxide (Fig. S2b) thereby offering higher resilience to moisture attack. The developed material also exhibited an n-type conductivity of 1.26 S cm^{-1} (Fig. 1i) whereas the pristine wide bandgap oxide was insulating (Fig. 1i), in accordance with the literature [49,50].

Theoretical calculations were also performed to reveal the properties of the developed material. The bulk structure of TaO_2F is cubic with space group of $Pm\bar{3}m$ [51,52]. The crystallographic refinement of O/F ratio on the shared site is 0.6667:0.3333, implying a disordered composition (partially occupied) but maintained stoichiometry. Prior to examining the electronic structure and binding energies of a single gaseous C atom trapped in a TaO_2F lattice, a full occupancy model without modifying the overall composition was considered. Three possible models (Fig. S10) were identified. The lattice energies of three structures were compared through the geometry optimizations of ion positions and cell parameters. Simulations determined that all three structures exhibit similar energies, suggesting that all three structures are identical. To consider the most favourable scenario of an interstitial C atom in the non-defective structure I, we generated a 3� 3�3 supercell consisting of 108 atoms. Fig. S11 shows the relaxed supercell structure and its density of state (DOS) plot. Calculations revealed that bulk TaO_2F exhibits approximately 3.0 eV band gap. Various possible interstitial positions were considered, and four promising relaxed structures were identified. Geometry-optimised structures together with a view of C interstitials are shown in Fig. S12.

In the first configuration (P), C is in the centre of the cubic motif without forming remarkable bonds with O or F (Fig. S12). This finding is reflected in the calculated bond distances and the almost zero Bader charge [51]. A small distortion in the lattice was observed. The binding energy is −0.60 eV, suggesting that the C in this interstitial position is more stable than its isolated gaseous atom. Interstitial C introduces a peak at the top of the VB without altering the band gap, making this material non-defective as indicated by UPS. Charge density around C is shown in Fig. 2. The second configuration (Q) consists of an interstitial C along the *bc* plane with a notable interaction with O and F (Table S1 and Fig. S12). This finding is also reflected in the Bader charge and relatively short bond distances. The interstitial C becomes slightly positive. The attractive interaction of C to O is slightly stronger compared with that to F based on the bond distances. The binding energy of C for the formation of this configuration is −0.20 eV, which is less favourable than that of configuration P. However, an important binding was observed in configuration R. In this configuration, C forms four short bonds with O and lies on the *ac* plane. On the contrary, F is further away from C, and its interaction with C is weak as observed in the C–F distances. Binding energy is −1.15 eV, which is more exoergic than that observed in P and Q. Strong binding is reflected in the Bader charge (slightly more positive than that noted in P and Q) and charge density around C and its neighbouring atoms (Fig. 2). The fourth configuration (S) exhibits the strongest interaction between C and O in the lattice. The binding energy is −5.89 eV, indicating a significant interaction with the lattice. Fig. S12 shows the strong bonding interaction between C and O. This finding is reflected in the shortest C–O bond distance (1.29 Å). A distortion in the lattice with F atoms moving slightly further away was observed. DOS and atomic DOS plots clearly show that the peak introduced by C is now mixed with the VB. Strong bonding interaction is also reflected in the charge density plot.

To explore the potential applicability of the novel compound in optoelectronic devices we then deposited a ~6 nm-thick TaO_2FC_x film (Fig. S13) on top of the green emissive conjugated co-polymer (F8BT) to evaluate its electron injection/transport capability in OLEDs. The alteration of the surface topography of F8BT (Fig. S14) and the detection of Ta 4f XPS peaks on F8BT (Fig. S15) indicate the successful deposition of the ternary compound on top of F8BT. The regular OLED configuration (Fig. S16) consists of an ITO transparent anode (100 nm thick), a 40 nm-thick PEDOT-PSS film as the hole transport layer, the emissive layer (F8BT or the blue emitting CN-PPP, the ETL and the aluminum cathode. In the reference devices, a commonly used Cs_2CO_3 film served as ETL for comparison reasons. Fig. S17 presents the energy level diagram of the materials used in the OLED structures (considering vacuum level alignment before contact). The VB and conduction band (CB) edges of TaO_2FC_x were estimated from UPS and absorption measurements, whereas the energy levels of the other OLED materials were obtained from literature [53]. The estimated CB value of 3.95 (±0.1) eV for TaO_2FC_x is expected to be highly beneficial for electron transport because it is located between the lowest unoccupied molecular orbital (LUMO) of the emissive layers and the Al cathode W_F, thus forming a type II heterojunction with F8BT. Fig. 3a presents the current density–voltage–luminance (J–V–L) characteristics of the F8BT-based OLEDs. Fig. 3b, Fig. S18 and Fig. 3c show the current, power and external electroluminescence (EL) quantum efficiency of OLEDs versus the current density, respectively. Table S2 summarises the OLEDs performance characteristics, which are highly improved when TaO_2FC_x was incorporated as the ETL instead of Cs_2CO_3. The C-doped TaO_2F-modified device exhibits an ultra-low turn-on voltage (2.0 eV) that is even lower than the F8BT's bandgap (Fig. S19), indicating a highly improved electron injection. This result was also proven by the current

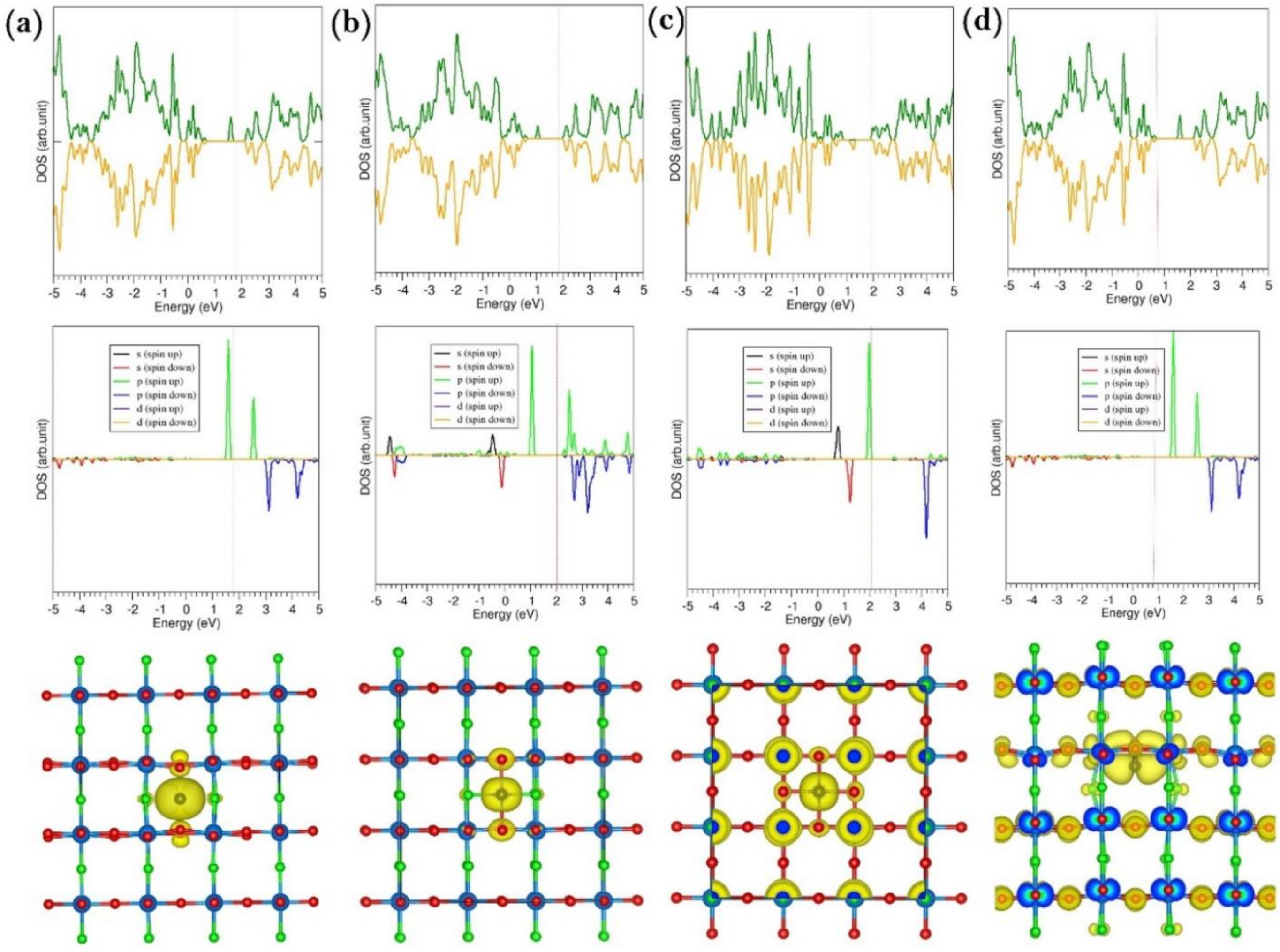

Fig. 2. Total DOS plots, Atomic DOS for C and constant charge density plots associated with C in the relaxed configurations. Plots a, b, c, and d, correspond to the configurations P, Q, R and S respectively.

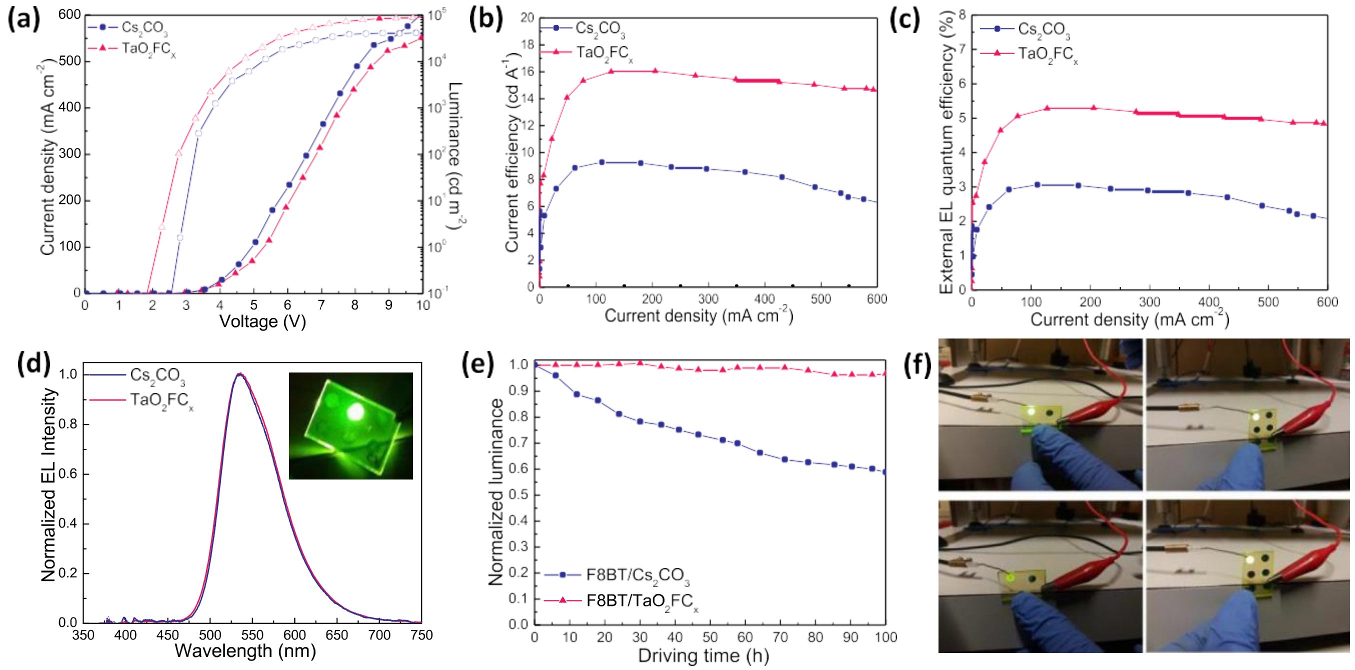

Fig. 3. (a) Current density and luminance versus voltage (J—V—L) characteristics, (b) current efficiency and (c) external EL quantum efficiency versus current density of the F8BT-based OLEDs using either Cs_2CO_3 or TaO_2FC_x films as the ETL. (d) The EL spectra of the corresponding devices at an applied voltage of 6 V. (e) Lifetime measurements: Normalized luminance versus driving time of the F8BT-based OLEDs at a constant current density of 15 mA cm^{-2}. (f) Photographs of the working OLEDs having Cs_2CO_3 (left) and TaO_2FC_x (right) as the electron selective contacts at 0 h (up) and 100 h (down) of constant operation.

density–voltage (J–V) characteristics of electron-only devices (Fig. S20). The achieved current efficiency of 16.53 cd/A is one of the highest ever for OLEDs using a thin (approximately 70 nm) F8BT layer [54,55]. The EL spectra are extremely similar to the photoluminescence emission spectrum of F8BT (Fig. 3d and Fig. S19a), suggesting that EL emission originates from the excitons that are generated exclusively inside F8BT. The hybrid oxide works as an effective ETL even in blue OLEDs (Fig. S21) where a CN-PPP co-polymer was used as the emitter. As one of the major issues in OLEDs is their operational stability, we measured operational lifetime for both reference (with Cs_2CO_3) and TaO_2FC_x-modified F8BT-based OLEDs in ambient. We note that whereas the reference device retained lower than 60% of its initial luminance after 100 h of continuous operation in air (biased at 15 mA cm^{-2}), the device with the C-doped Ta dioxyfluoride ETL retained above 90% of its initial luminance (Fig. 3e and f). This is due to the superior quality of the modified cathode interface and its high robustness and hydrophobicity that act as a protective layer against moisture ingress into the device. UPS measurements obtained on a F8BT film prior to (Fig. S22) and after the deposition of TaO_2FC_x on top (Fig. 4a) revealed a remarkable decrease in the electron injection barrier from 1.1 eV (Figure 4b) to 0.3 eV (Fig. 4c), which explains the superiority of the ternary compound as an electron injection/transport layer. This large reduction in the electron injection barrier enhances the electron injection/transport from the Al cathode to F8BT and improves the quality of the cathode interface; injection barriers 0–0.4 eV indicate the formation of an Ohmic rather than a Schottky contact [56].

To further explore the versatility of TaO_2FC_x in other organic optoelectronic devices, we fabricated single junction binary OSCs with the regular architecture. These devices employed blends of either PTB7-Th: $PC_{71}BM$ (fullerene OSCs) or (PM6:IT-4F) (non-fullerene OSCs) (Fig. S23). The control devices included the well-established PDINO as ETL deposited on top of the photoactive blend. For the PTB7-Th: $PC_{71}BM$-based OSCs, a considerable improvement in power conversion efficiency (PCE) up to 10.48% was obtained by the TaO_2FC_x-modified device compared with the reference device with the PDINO (PCE up to 9.40%) (Fig. S24 and Table S3). The enhanced OSC performance can be attributed to the high quality of the cathode contact as indicated by the low trap-assisted/mono-molecular recombination (Fig. S25) and improved electron transport in the photoactive blend (Fig.S26 and Table S4) of the TaO_2FC_x-based device [57]. Added to the merits is the high long-term stability of the “self-encapsulated” TaO_2FC_x-modified devices. This characteristic is directly related to the robustness and hydrophobic nature of the ternary material. The appropriate position of the CB edge of TaO_2FC_x is expected to facilitate electron extraction not only from the LUMO of $PC_{71}BM$ (~3.9 eV) but also from the LUMOs of the recently developed non-fullerene acceptors (located ~ 4.0 eV) (Fig. 5a) towards Al by acting as an intermediate energy step. As a result, the PM6:IT-4F based OSC with a regular architecture ITO/PEDOT-PSS/PM6:IT-4F/ETL/Al and the TaO_2FC_x as ETL reached a high maximum PCE of 13.18% (Fig. 5b and Table S5) and an average PCE of 12.77% (Fig. 5c), indicating a remarkable enhancement relative to that of the control device with PDINO (PCE$_{max}$¼ 12.04%). The enhanced photon-to-electron conversion efficiency (Fig. 5d) and improved electron transport (Fig. 5d and Table S6 with the calculated electron mobilities) revealed the high quality of cathode interface in this device configuration. The incorporation of TaO_2FC_x also contributes to the excellent stability of the device when exposed to UV light under ambient conditions (Fig. 5f). The performance is further enhanced in OSCs with the inverted architecture FTO/ETL (40 nm)/PM6:IT-4F/-MoO_x/Al using our developed material (or the widely used ZnO as reference) as the bottom ETL. The control device (with the ZnO ETL) shows a high efficiency (reaching a maximum PCE of 13.03%) which, however, is lower compared with the TaO_2FC_x one (PCE$_{max}$¼ 14.14%) because of the advantages of the ternary material discussed above. This finding represents one of the high efficiencies of single junction PM6: IT-4F-based OSCs currently reported [58,59]. The high UV–Vis absorption of the PM6:IT-4F film on top of TaO_2FC_x (Fig. S27) is assigned to the high transmittance (lower absorption) of the cathode contact, the absence of trap states on the surface of the ternary compound (Fig. S28) and the improved nanomorphology of the photoactive layer due to the

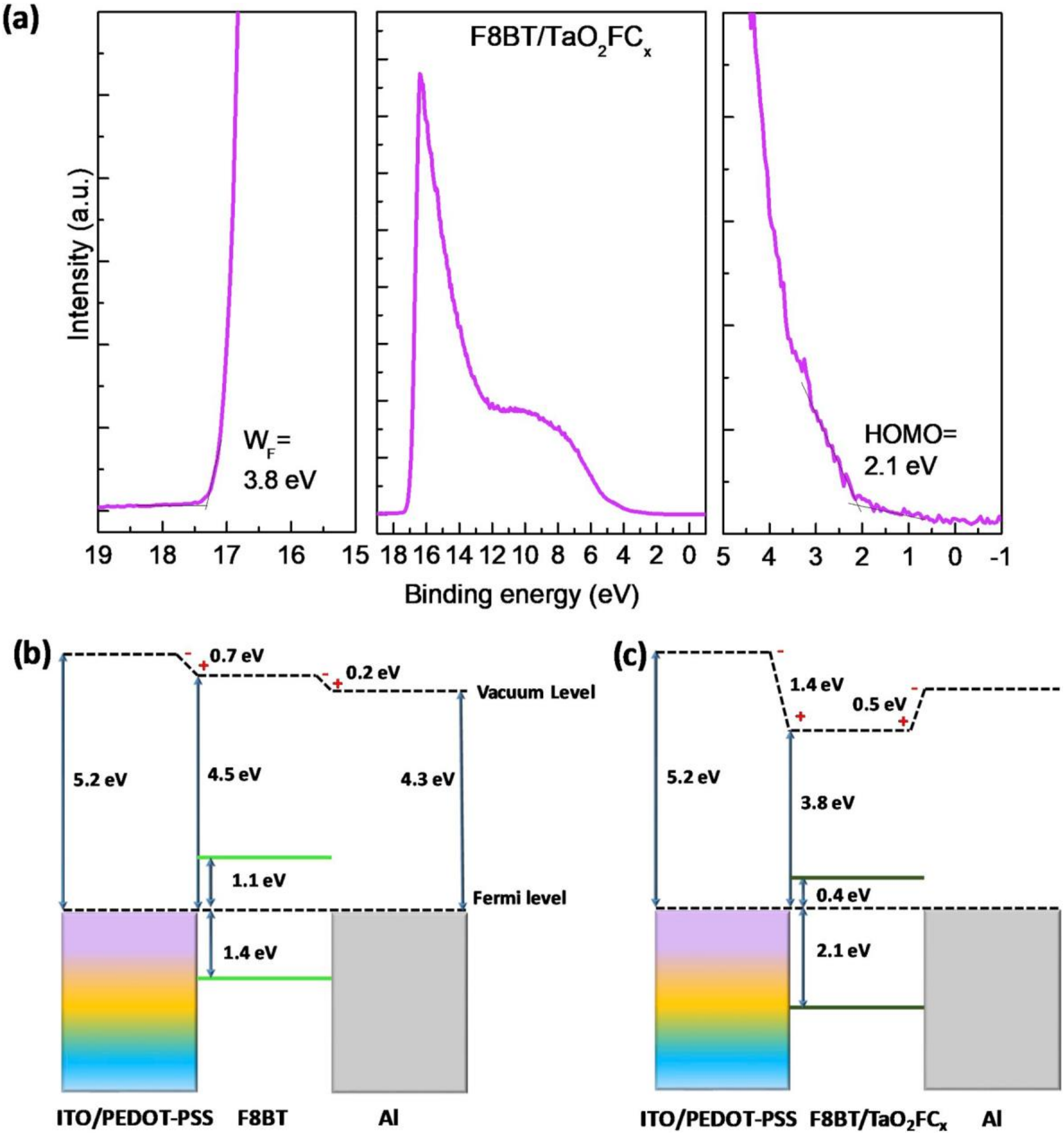

Fig. 4. (a) UPS spectra (left: the high binding energy cut-off, middle: an expanded view and right: the near Fermi level region) of an F8BT film deposited on PEDOT-PSS on ITO/glass substrate after the deposition of the TaO$_2$FC$_x$ film. The corresponding energy level diagram of the OLED devices with the configuration (b) ITO/PEDOT-PSS/F8BT/Al and (c) ITO/PEDOT-PSS/F8BT/TaO$_2$FC$_x$/Al, assuming a constant Fermi level at thermodynamic equilibrium.

higher hydrophobicity of TaO$_2$FC$_x$ compared with that of ZnO (Fig. S29). All these observations verify the superior role of the C-doped TaO$_2$F as an advanced electron transport material (Tables S8–S10 demonstrated a comparison between the efficiencies of the organic optoelectronics demonstrated herein with similar devices in the literature) and open a new era for the application of non-defective oxide-based materials in optoelectronic devices.

4. Conclusions

In summary, we developed an efficient electron transport material for optoelectronic applications through a simple and low-cost deposition method. We incorporated the novel compound, namely carbon-doped tantalum dioxyfluoride, in many types of organic optoelectronic devices and we obtained among others green fluorescent OLEDs with a regular architecture reaching current efficiencies of 16.53 cd/A and non-fullerene OSCs with an inverted architecture reaching PCEs of 14.14%. All these devices exhibited the additional advantage of high operational and temporal stability due to the self-encapsulation effect of the highly hydrophobic TaO$_2$FC$_x$. Our methodology on the preparation of ternary oxides with desired properties, such as TaO$_2$FC$_x$, can easily be extended to other simple and well-established deposition techniques, including solution-processing, to enable the low-cost development of C-doped metal oxyfluoride semiconductors and beyond. This study may open new avenues and create opportunities for research in organic materials, Si, perovskite, quantum-dot solar cells and light-emitting devices.

Intellectual property

We confirm that we have given due consideration to the protection of intellectual property associated with this work and that there are no impediments to publication, including the timing of publication, with respect to intellectual property. In so doing we confirm that we have

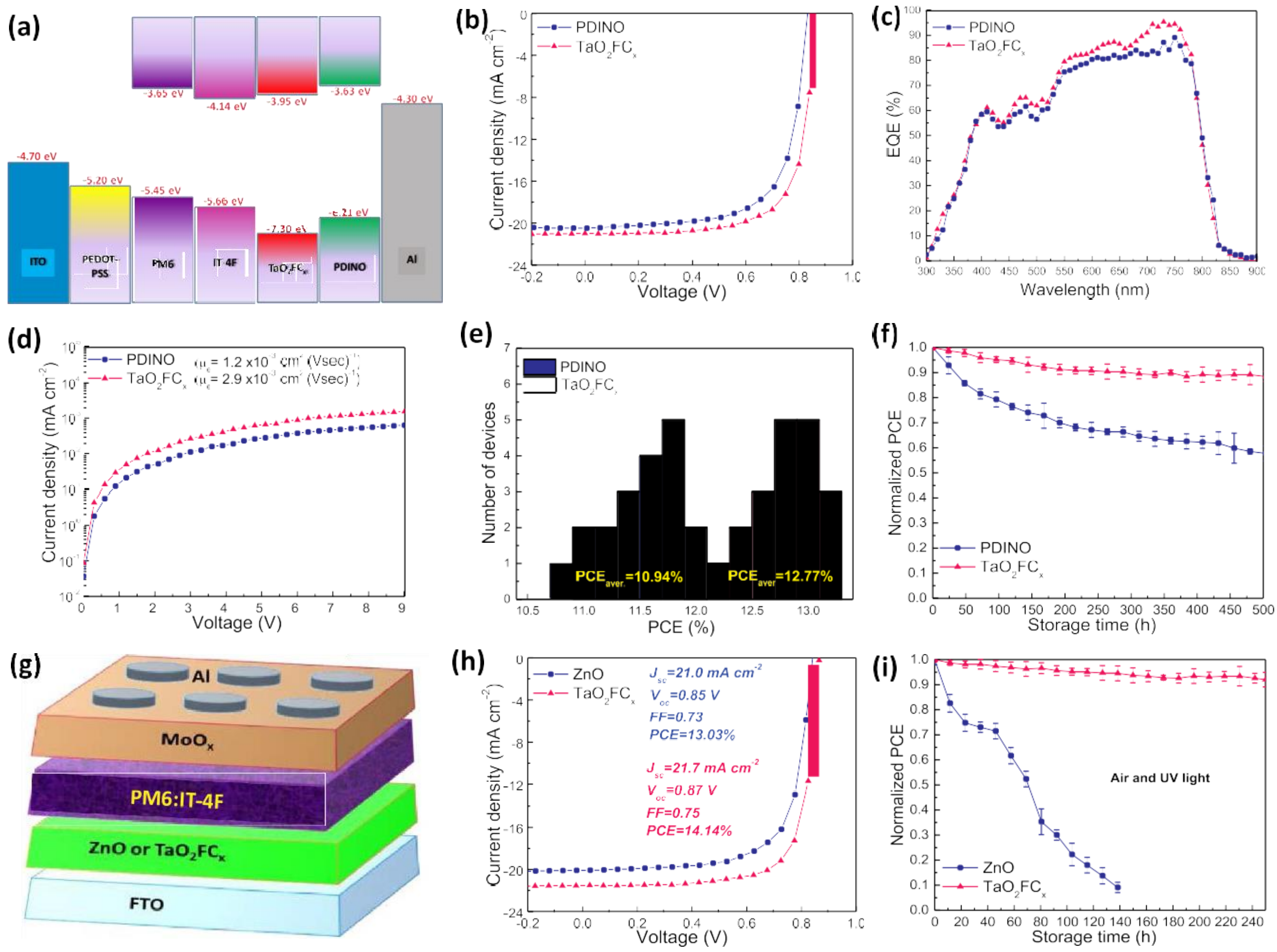

Fig. 5. (a) The energy levels of the materials used in the PM6:IT-4F OSCs (before contact, considering vacuum level alignment). (b) J-V characteristic curves taken under 1.5 A.M. illumination and (c) EQE spectra of PM6:IT-4F based OSCs. (d) The J-V characteristics of electron-only devices, (e) the PCE statistics and (f) variation of PCE versus storage time of unencapsulated devices. (g) The inverted OSC architecture, (h) J-V under 1.5 A.M. illumination of the devices shown in (g) and (i) The variation of PCE of unencapsulated inverted devices versus time in air under UV illumination.

followed the regulations of our institutions concerning intellectual property.

Research ethics

We further confirm that any aspect of the work covered in this manuscript that has involved human patients has been conducted with the ethical approval of all relevant bodies and that such approvals are acknowledged within the manuscript.

Funding

All of the sources of funding for the work described in this publication are acknowledged below: X. B. thanks the Youth Innovation Promotion Association CAS (2016194) for financial support.

Declaration of competing interest

We wish to confirm that there are no known conflicts of interest associated with this publication and there has been no significant financial support for this work that could have influenced its outcome.

Acknowledgements

High Performance Computing Centres at Imperial College London and Coventry University are acknowledged for rending computational facilities and support to run DFT calculations. X. B. thanks the Youth Innovation Promotion Association CAS (2016194) for financial support.

Appendix A. Supplementary data

Additional material and device characterization and theoretical calculations.

Supplementary data to this article can be found online at https://doi.org/10.1016/j.nanoen.2020.104508.

References

[1] Q. Wang, M. Nakabayashi, T. Hisatomi, S. Sun, S. Akiyama, Z. Wang, Z. Pan, X. Xiao, T. Watanabe, T. Yamada, N. Shibata, T. Takata, K. Domen, Oxysulfide photocatalyst for visible-light-driven overall water splitting, Nat. Mater. 18 (2019) 827–832.

[2] C.R. Bala, S. Breen, Y. Shao, S. Ardo, A.Z. Weber, Evaluating particle-suspension reactor designs for Z-scheme solar water splitting via transport and kinetic modeling, Energy Environ. Sci. 11 (2018) 115–135.

[3] J.H. Burroughes, D.D.C. Bradley, A.R. Brown, R.N. Marks, K. Mackay, R.H. Friend, P.L. Burns, A.B. Holmes, Light-emitting diodes based on conjugated polymers, Nature 347 (1990) 539–541.

[4] S.R. Forrest, The path to ubiquitous and low-cost organic electronic appliances on plastic, Nature 428 (2004) 911–918.

[5] Z. He, B. Xiao, F. Liu, H. Wu, Y. Yang, S. Xiao, C. Wang, T.P. Russell, Y. Cao, Single-junction polymer solar cells with high efficiency and photovoltage, Nat. Photonics 9 (2015) 174–179.

[6] G. Li, R. Zhu, Y. Yang, Y, Polymer solar cells, Nat. Photonics 6 (2012) 153–161.

[7] C.-C. Chueh, C.-Z. Li, A.K.Y. Jen, Recent progress and perspective in solution-processed interfacial materials for efficient and stable polymer and organometal perovskite solar cells, Energy Environ. Sci. 8 (2015) 1160–1189.

[8] F. Wang, Z.A. Tan, Y. Li, Solution-processable metal oxides/chelates as electrode buffer layers for efficient and stable polymer solar cells, Energy Environ. Sci. 8 (2015) 1059–1091.

[9] Z. Yin, J. Wei, Q. Zheng, Interfacial materials for organic solar cells: recent advances and perspectives, Adv. Sci. 3 (2016) 1500362.

[10] Y. Zhou, C. Fuentes-Hernandez, J. Shim, J. Meyer, A.J. Giordano, H. Li, P. Winget, T. Papadopoulos, H. Cheun, J. Kim, M. Fenoll, A. Dindar, W. Haske, E. Najafabadi, T.M. Khan, H. Sojoudi, S. Barlow, S. Graham, J.-L. Brédas, S.R. Marder, A. Kahn, B. Kippelen, A universal method to produce low–work function electrodes for organic electronics, Science 336 (2012) 327–332.

[11] T.-H. Lai, S.-W. Tsang, J.R. Manders, S. Chen, F. So, Properties of interlayer for organic photovoltaics, Mater. Today 16 (2013) 424–432.

[12] W. Zhao, S. Li, H. Yao, S. Zhang, Y. Zhang, B. Yang, J. Hou, Molecular optimization enables over 13% efficiency in organic solar cells, J. Am. Chem. Soc. 139 (2017) 7148–7151.

[13] M. Vasilopoulou, E. Polydorou, A.M. Douvas, L.C. Palilis, S. Kennou, P. Argitis, Annealing-free highly crystalline solution-processed molecular metal oxides for efficient single-junction and tandem polymer solar cells, Energy Environ. Sci. 8 (2015) 2448–2463.

[14] C.V. Hoven, R. Yang, A. Garcia, V. Crockett, A.J. Heeger, G.C. Bazan, T.-Q. Nguyen, Electron injection into organic semiconductor devices from high work function cathodes, Proc. Natl. Acad. Sci. U. S. A 105 (2018) 12730–12735.

[15] C. Murawski, K. Leo, M. Gather, Efficiency roll-off in organic light-emitting diodes, Adv. Mater. 25 (2013) 6801–6827.

[16] B.R. Lee, S. Lee, J.H. Park, E.D. Jung, J.C. Yu, Y.S. Nam, J. Heo, J.-Y. Kim, B.-Su Kim, M.H. Song, Amine-based interfacial molecules for inverted polymer-based optoelectronic devices, Adv. Mater. 27 (2015) 3553–3559.

[17] C. Hoven, R. Yang, A. Garcia, A.J. Heeger, T.-Q. Nguyen, G.C. Bazan, Ion motion in conjugated polyelectrolyte electron transporting layers, J. Am. Chem. Soc 129 (2007) 10976–10977.

[18] T. Kim, M. Suh, S.J. Kwon, T.H. Lee, J.E. Kim, Y.J. Lee, J.H. Kim, M. Hong, K. S. Suh, Poly(3,4ethylenedioxythiophene) derived from poly(ionic liquid) for the use as hole-injecting material in organic light-emitting diodes, Macromol. Rapid Commun. 30 (2009) 1477–1482.

[19] L.P. Lu, D. Kabra, R.H. Friend, Barium hydroxide as an interlayer between zinc oxide and a luminescent conjugated polymer for light-emitting diodes, Adv. Funct. Mater. 22 (2012) 4165–4171.

[20] Lange, I. et al I. Lange, S. Reiter, M. Pätzel, A. Zykov, A. Nefedov, J. Hildebrandt, S. Hecht, S. Kowarik, C. Wöll, G. Heimel, D. Neher, Tuning the work function of polar zinc oxide surfaces using modified phosphonic acid self-assembled monolayers, Adv. Funct. Mater. 24 (2014) 7014–7024.

[21] M. Liu, M.B. Johnston, H.J. Snaith, Efficient planar heterojunction perovskite solar cells by vapour deposition, Nature 501 (2013) 395–398.

[22] M. Abuhelaiqa, S. Paek, Y. Lee, K.T. Cho, S. Heo, E. Oveisi, A.J. Huckaba, H. Kanda, H. Kim, Y. Zhang, R. Humphry-Baker, S. Kinge, A.M. Asiri, M.K. Nazeeruddin, Stable perovskite solar cells using tin acetylacetonate based electron transporting layers, Energy Environ. Sci. 12 (2019) 1910–1917.

[23] A. Fakharuddin, L. Schmidt-Mende, G. Garcia-Belmonte, R. Jose, I. Mora-Sero, Interfaces in perovskite solar cells, Adv. Energy Mater. 7 (2017) 1700623.

[24] S.S. Shin, E.J. Yeom, W.S. Yang, S. Hur, M.G. Kim, J. Im, J. Seo, J.H. Noh, S.I. Seok, Colloidally prepared La-doped $BaSnO_3$ electrodes for efficient, photostable perovskite solar cells, Science 356 (2017) 167–171.

[25] A. Pérez-Tomas, H. Xie, Z. Wang, H.-S. Kim, I. Shirley, S.-H. Turren-Cruz, A. Morales-Melgares, B. Saliba, D. Tanenbaum, M. Saliba, S.M. Zakeeruddin, M. Gratzel, A. Hagfeldt, M. Lira-Cantu, $PbZrTiO_3$ ferroelectric oxide as an electron extraction material for stable halide perovskite solar cells, Sustain. Energy Fuels 3 (2019) 382–389.

[26] X. Yu, T.J. Marks, A. Facchetti, Metal oxides for optoelectronic applications, Nat. Mater. 15 (2016) 383–396.

[27] C. Li, T. Wang, Z. Luo, D. Zhang, J. Gong, Transparent ALD-grown Ta_2O_5 protective layer for highly stable ZnO photoelectrode in solar water splitting, Chem. Commun. 51 (2015) 7290–7293.

[28] Y. Wan, S.K. Karuturi, C. Samundsett, J. Bullock, M. Hettick, D. Yan, J. Peng, P. R. Narangari, S. Mokkapati, H.H. Tan, C. Jagadish, A. Javey, A. Cuevas, Tantalum oxide electron-selective heterocontacts for silicon photovoltaics and photoelectrochemical water reduction, ACS Energy Lett 31 (2018) 125–131.

[29] R. Nakamura, T. Tanaka, Y. Nakato, Oxygen photoevolution on a tantalum oxynitride photocatalyst under visible-light irradiation: How does water photooxidation proceed on a metal-oxynitride surface? J. Phys. Chem. B 109 (2005) 8920–8927.

[30] H. Tu, L. Xu, F. Mou, J. Guan, Single crystalline tantalum oxychloride microcubes: controllable synthesis, formation mechanism and enhanced photocatalytic hydrogen production activity, Chem. Commun. 51 (2015) 12455–12458.

[31] X. Yue, Y. Jin, P.K. Shen, Highly stable and efficient non-precious metal electrocatalysts of tantalum dioxyfluoride used for the oxygen evolution reaction, J. Mater. Chem. A 5 (2017) 8287–8291.

[32] X. Yue, C. He, C. Zhong, Y. Chen, S.P. Jiang, P.K. Shen, Fluorine-doped and partially oxidized tantalum carbides as nonprecious metal electrocatalysts for methanol oxidation reaction in acidic media, Adv. Mater. 28 (2016) 2163–2169.

[33] D.M. Antonelli, J.Y. Ying, Synthesis and characterization of hexagonally packed mesoporous tantalum oxide molecular sieves, Chem. Mater. 8 (1996) 874–881.

[34] L. Shen, X. Zhou, X. Zhang, Y. Zhang, Y. Liu, W. Wang, W. Si, X. Dong, Carbon-intercalated $Ti_3C_2T_x$ MXene for high performance electrochemical energy storage, J. Mater. Chem. A 6 (2018) 23513–23520.

[35] S. Zhang, Y. Qin, J. Zhu, J. Hou, Over 14% Efficiency in polymer solar cells enabled by a chlorinated polymer donor, Adv. Mater. 30 (2018) 1800613.

[36] N. Vourdas, G. Papadimitropoulos, I. Kostis, M. Vasilopoulou, D. Davazoglou, Substoichiometric hot-wire WOx films deposited in reducing environment, Thin Solid Films 520 (2012) 3614–3619.

[37] M. Vasilopoulou, I. Raptis, P. Argitis, I. Aspiotis, D. Davazoglou, Polymeric electrolytes for WO_3-based all solid-state electrochromic displays, Microelectron. Eng. 83 (2006) 1414–1417.

[38] S. Grimme, J. Antony, S. Ehrlich, H. Krieg, A consistent and accurate ab initio parametrization of density functional dispersion correction (DFT-D) for the 94 elements H-Pu, J. Chem. Phys. 132 (2010) 154104.

[39] E. Polydorou, I. Sakellis, A. Soultati, A. Kaltzoglou, T.A. Papadopoulos, J. Briscoe, D. Tsikritzis, M. Fakis, L.C. Palilis, S. Kennou, P. Argitis, P. Falaras, D. Davazoglou, M. Vasilopoulou, Avoiding ambient air and light induced degradation in high-efficiency polymer solar cells by the use of hydrogen-doped zinc oxide as electron extraction material, Nano Energy 34 (2017) 500–514.

[40] K.Y. Yiang, W.J. Yoo, Investigation of electrical conduction in carbon-doped silicon oxide using a voltage ramp method, Appl. Phys. Lett. 83 (2003) 524–526.

[41] Y. Abbas, Y.-R. Jeon, A.S. Sokolov, S. Kim, B. Ku, C. Choi, Compliance-free, digital SET and analog RESET synaptic characteristics of sub-tantalum oxide based neuromorphic device, Sci. Rep. 8 (2018) 1228.

[42] Y. Xin, P.K. Shen, Tantalum carbide doped by fluorine as non-precious metal anodic electrocatalyst superior to Pt/C for glycerol-oxidation, Electrochim. Acta 227 (2017) 267–274.

[43] R. Simpson, R.G. White, J.F. Watts, M.A. Baker, XPS investigation of monatomic and cluster argon ion sputtering of tantalum pentoxide, Appl. Surf. Sci. 405 (2017) 79–87.

[44] T. Horikawa, N. Sakao, T. Sekida, J. Hayashi, D.D. Doc, M. Katoh, Preparation of nitrogen-doped porous carbon by ammonia gas treatment and the effects of N-doping on water adsorption, Carbon 50 (2012) 1833–1842.

[45] A. Agulyansky, The Chemistry of Tantalum and Niobium Fluoride Compounds, Elsevier, Boston, 2004, p. 8.

[46] L.K. Frevel, H.W. Rinn, The crystal structure of NbO_2F and TaO_2F, Acta Crystallogr. 9 (1956) 626–627.

[47] V. Gutman, K.H. Jack, The crystal structures of molybdenum trifluoride, MoF_3, and tantalum trifluoride, TaF_3, Acta Crystallogr. 4 (1951) 244–246.

[48] J.C. Biffinger, H.W. Kim, The polar hydrophobicity of fluorinated compounds, Chembiochem 5 (2004) 622–627.

[49] I. Hodgkinson, Q.h. Wu, J. Hazel, Empirical equations for the principal refractive indices and column angle of obliquely deposited films of tantalum oxide, titanium oxide, and zirconium oxide, Appl. Opt. 37 (1993) 2653–2659.

[50] L. Liu, Z. Mei, Y. Hou, H. Liang, A. Azarov, V. Venkatachalapathy, A. Kuznetsov, X. Du, Fluorine doping: a feasible solution to enhancing the conductivity of high-resistance wide bandgap $Mg_{0.51}Zn_{0.49}O$ active components, Sci. Rep. 5 (2015) 15516.

[51] G. Henkelman, A. Arnaldsson, H. Jónsson, A fast and robust algorithm for Bader decomposition of charge density, Comput. Mater. Sci. 36 (2006) 354–360.

[52] W. Tang, E. Sanville, G. Henkelman, G. A grid-based Bader analysis algorithm without lattice bias, J. Phys. Condens. Matter 21 (2009), 084204.

[53] D.G. Georgiadou, L.C. Palilis, M. Vasilopoulou, G. Pistolis, D. Dimotikali, P. Argitis, Effect of triphenylsulfonium triflate addition in wide band-gap polymer light emitting diodes: improved charge injection, transport and electroplex-induced emission tuning, RSC Adv. 2 (2012) 11786–11792.

[54] J. Zhao, Y. Cai, J.-P. Yang, H.-X. Wei, Y.-H. Deng, Y.-Q. Li, S.-T. Lee, J.-X. Tang, The role of cesium carbonate on the electron injection and transport enhancement in organic layer by admittance spectroscopy, Phys. Lett. 101 (2012) 193303.

[55] B.R. Lee, E.D. Jung, J.S. Park, Y.S. Nam, S.H. Min, B.-S. Kim, K.-M. Lee, J.-R. Jeong, R.H. Friend, J.-S. Kim, S.O. Kim, M.H. Song, Highly efficient inverted polymer light-emitting diodes using surface modifications of ZnO layer, Nat. Commun. 5 (2014) 4840.

[56] M. Sessolo, H.J. Bolink, Hybrid organic–inorganic light–emitting diodes, Adv. Mater. 23 (2011) 1829–1845.

[57] V. Papamakarios, E. Polydorou, A. Soultati, N. Droseros, D. Tsikritzis, A.M. Douvas, L. Palilis, M. Fakis, S. Kennou, P. Argitis, M. Vasilopoulou, Surface modification of ZnO layers via hydrogen plasma treatment for efficient inverted polymer solar cells, ACS Appl. Mater. Interfaces 8 (2016) 1194–1205.

[58] K. Vandewal, S. Albrecht, E.T. Hoke, K.R. Graham, J. Widmer, J.D. Douglas, M. Schubert, W.R. Mateker, J.T. Bloking, G.F. Burkhard, A. Sellinger, J.M. J. Fréchet, A. Amassian, M.K. Riede, M.D. McGehee, D. Neher, A. Salleo, Efficient charge generation by relaxed charge-transfer states at organic interfaces, Nat. Mater. 13 (2014) 63–68.

[59] J. Yuan, Y. Zhang, L. Zhou, G. Zhang, H.-L. Yip, T.-K. Lau, X. Lu, C. Zhu, H. Peng, P. A. Johnson, M. Leclerc, Y. Cao, J. Ulanski, Y. Li, Y. Zou, Single-junction organic solar cell with over 15% efficiency using fused-ring acceptor with electron-deficient core, Joule 3 (2019) 1140–1151.